UC Davis
UC Davis Previously Published Works

Title

Adaptive optics-optical coherence tomography: optimizing visualization of microscopic retinal structures in three dimensions.

Permalink

https://escholarship.org/uc/item/8qs9w27f

Journal

Journal of the Optical Society of America A, 24(5)

ISSN

1084-7529

Authors

Zawadzki, Robert J
Choi, Stacey S
Jones, Steven M
et al.

Publication Date

2007-05-01

DOI

10.1364/josaa.24.001373

Peer reviewed

eScholarship.org Powered by the California Digital Library
University of California

Adaptive optics–optical coherence tomography: optimizing visualization of microscopic retinal structures in three dimensions

Robert J. Zawadzki and Stacey S. Choi

Department of Ophthalmology and Vision Science, Vision Science and Advanced Retinal Imaging Laboratory, University of California Davis, 4860 Y Street, Suite 2400, Sacramento, California 95817, USA

Steven M. Jones and Scot S. Oliver

Lawrence Livermore National Laboratory, 7000 East Avenue, Livermore, California 94550, USA

John S. Werner

Department of Ophthalmology and Vision Science, Vision Science and Advanced Retinal Imaging Laboratory, University of California Davis, 4860 Y Street, Suite 2400, Sacramento, California 95817, USA

Received August 15, 2006; revised November 13, 2006; accepted December 18, 2006;
posted January 2, 2007 (Doc. ID 74082); published April 11, 2007

Adaptive optics–optical coherence tomography (AO-OCT) permits improved imaging of microscopic retinal structures by combining the high lateral resolution of AO with the high axial resolution of OCT, resulting in the narrowest three-dimensional (3D) point-spread function (PSF) of all *in vivo* retinal imaging techniques. Owing to the high volumetric resolution of AO-OCT systems, it is now possible, for the first time, to acquire images of 3D cellular structures in the living retina. Thus, with AO-OCT, those retinal structures that are not visible with AO or OCT alone (e.g., bundles of retinal nerve fiber layers, 3D mosaic of photoreceptors, 3D structure of microvasculature, and detailed structure of retinal disruptions) can be visualized. Our current AO-OCT instrumentation uses spectrometer-based Fourier-domain OCT technology and two-deformable-mirror-based AO wavefront correction. We describe image processing methods that help to remove motion artifacts observed in volumetric data, followed by innovative data visualization techniques [including two-dimensional (2D) and 3D representations]. Finally, examples of microscopic retinal structures that are acquired with the University of California Davis AO-OCT system are presented. © 2007 Optical Society of America

OCIS codes: 110.4500, 010.1080, 170.0110, 120.3890, 170.4470, 220.1000.

1. INTRODUCTION

Fourier-domain optical coherence tomography (FD-OCT)[1–8] is already on its way to revolutionizing clinical retinal imaging in research settings owing to its significant advantage in sensitivity and acquisition speed over the standard time-domain OCT technique.[9–11] FD-OCT allows for rapid acquisition of retinal images (without reduction in axial resolution), making it feasible for volumetric reconstruction of retinal structures with ultrahigh axial resolution.[12–14] Attempts to improve the lateral resolution of OCT to theoretical diffraction-limited performance have, however, been progressing more slowly. While axial resolution with OCT depends on the bandwidth of the imaging source, lateral resolution is limited by the eye's optical aberrations, including temporally varying higher-order aberrations. These aberrations can be corrected dynamically using adaptive optics (AO).

AO has been combined by Miller *et al.*[15] with time-domain-based *en-face* coherence-gated OCT and by Hermann *et al.*[16] with time-domain ultrahigh-resolution (UHR)-OCT. Later, AO was combined with FD-OCT by Zhang *et al.*[17] using a line-illumination approach followed by several reports of three-dimensional (3D) confocal AO-OCT imaging[18–20] and C-scan time-domain OCT.[21] Interestingly, one of the main features that distinguishes OCT from other imaging modalities (independence of axial and lateral resolution) is lost in retinal AO-OCT systems. As theoretically predicted by Fernández and Drexler,[22] for a given imaging pupil diameter, increasing axial resolution of AO-OCT (increasing spectral bandwidth of the light source) decreases lateral resolution. This effect is due to the chromatic aberration of the eye and is more pronounced for larger pupil diameters even if monochromatic aberrations are fully corrected. This problem has not been noted for UHR-OCT systems, but it has become important for AO-OCT systems. Thus, unless chromatic aberration is corrected,[23] the maximum spectral bandwidth (axial resolution) that does not compromise lateral resolution is dependent on the eye's pupil diameter used for imaging. This consideration has influenced our choice of parameters for our current AO-OCT system design.

This paper describes the University of California (UC) Davis two-deformable-mirror (DM) AO-OCT system that is capable of *in vivo* imaging of 3D microscopic retinal structures with high lateral (up to 3 μm) and high axial ($\sim$6 μm) resolution. Our AO subsystem utilizes two DMs:

1084-7529/07/051373-11/$15.00 © 2007 Optical Society of America

a 37-element bimorph DM and 144-element micro-electromechanical system (MEMS) DM working in a closed loop. The large stroke of the bimorph DM reduces the need for trial lens correction of individual refractive error [up to ±3 diopters (D) defocus and ±1 D cylinder], which is important for OCT because trial lenses produce unequal dispersion in the sample and reference channels. Another advantage of using two DMs is that the focus of the AO correction can be varied within the retina using only one of the DMs (bimorph mirror), leaving the full dynamic range of the second mirror for AO correction. The primary purpose of this paper is not, however, to discuss the benefits and complications associated with use of a two-DM-based AO system. Instead, the major focus is on AO-OCT image processing steps that improve image quality and reduce motion artifacts in volumetric data. Custom software provides innovative approaches to data visualization [including two-dimensional (2D) and 3D representations], which we demonstrate for microscopic retinal structures, including foveal microvasculature, bundles within the retinal nerve fiber layer, 3D photoreceptor mosaic, and drusen in a retina with age-related macular degeneration.

2. METHODS

We first briefly summarize the current configuration of our AO-OCT system and then describe techniques for data acquisition, processing, and visualization.

A. Experimental System

Figure 1 shows a schematic of our AO-OCT system. Some of the components of this system have been previously described by Laut *et al.*[24] and Zawadzki *et al.*[19]; however, the MEMS DM used in this work has mechanical dimensions smaller than those previously reported. This has required changes in the optical design of the sample arm, accomplished by replacing two telescopes close to the MEMS DM with magnification factors changed from $\gamma'_{3,4}=2.4$ and $\gamma'_{5,6}=1.5$ to $\gamma_{3,4}=3.2$ and $\gamma_{5,6}=1.16$, respectively. The length of the OCT reference arm has been modified accordingly to accommodate for the path-length difference in the sample arm, ensuring the proper location of the subject's eye pupil [at the plane conjugated to the X and Y scanning mirrors, both wavefront correctors, and Hartmann–Shack (H-S) wavefront sensor]. The system currently uses a 90/10 fiber coupler (90% reference, 10% sample), improving the throughput of the light backscattered from the eye to the detector. The light source was a fiber-pigtailed superluminescent diode from Superlum Ltd. (Moscow, Russia) with the central wavelength located at 840 nm (FWHM=50 nm). The measured axial resolution was 6 μm in the retina. A water cuvet was placed in the reference arm to compensate for the subject's eye dispersion. The magnification factors, γ, between the eye pupil plane and the conjugated DM planes were chosen to best fit the physical dimensions of both DMs [~10 mm diameter pupil image for the AOptix bi-

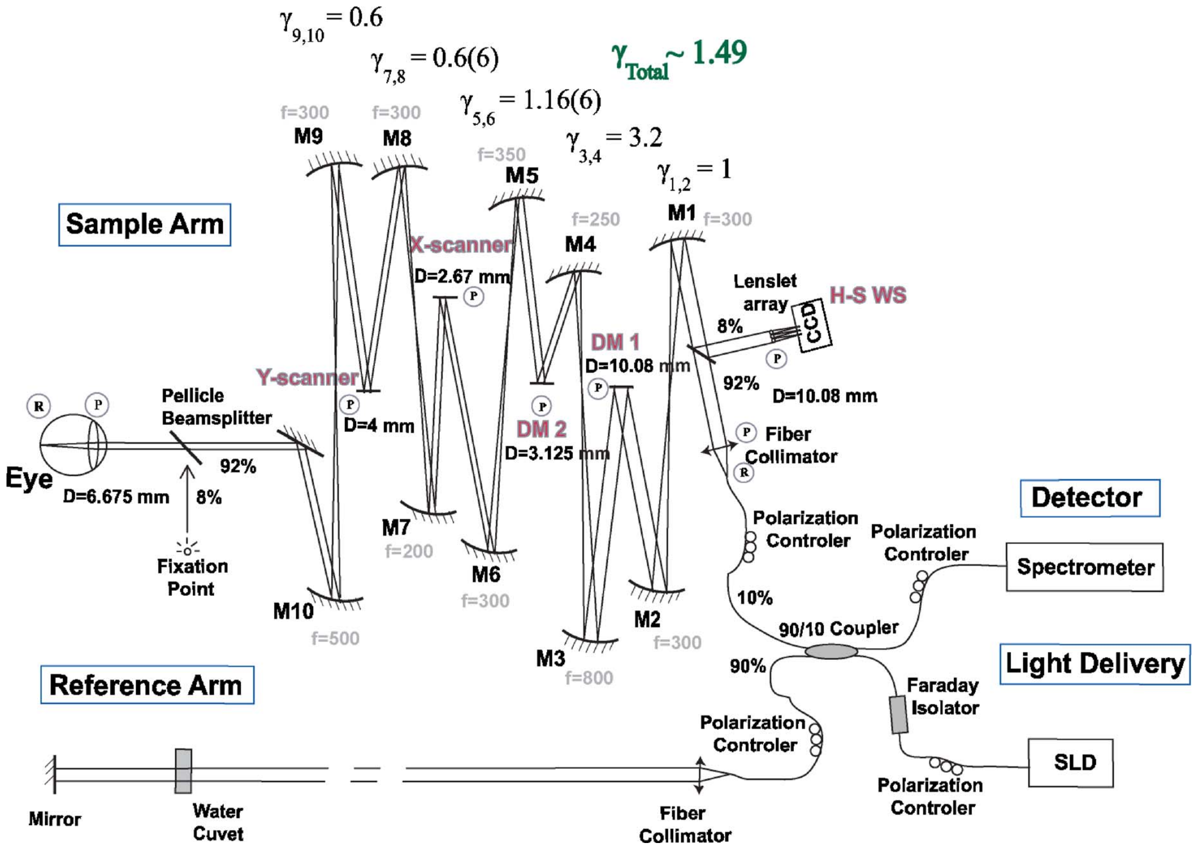

$\gamma_{9,10}=0.6$
$\gamma_{7,8}=0.6(6)$
$\gamma_{\text{Total}}\sim 1.49$
$\gamma_{5,6}=1.16(6)$
$\gamma_{3,4}=3.2$
$\gamma_{1,2}=1$
f=300
M9
f=300
M8
f=350
M5
f=250
M4
M1
f=300
Sample Arm
X-scanner
D=2.67 mm
P
Lenslet array
H-S WS
CCD
8%
DM 1
D=10.08 mm
P
92%
D=10.08 mm
Y-scanner
P
D=4 mm
P
DM 2
D=3.125 mm
P
P
Fiber Collimator
R
R
P
Pellicle Beamsplitter
92%
Eye
D=6.675 mm
8%
Fixation Point
M7
f=200
M6
f=300
M10
f=500
M3
f=800
M2
f=300
Polarization Controler
Polarization Controler
Detector
Spectrometer
10%
90/10 Coupler
90%
Light Delivery
Faraday Isolator
Reference Arm
Polarization Controler
SLD
Polarization Controler
Mirror
Water Cuvet
Fiber Collimator

Fig. 1. (Color online) Schematic of AO-OCT system. "R" and "P" denote retinal and pupil planes, respectively. DM1, bimorph deformable mirror (AOptix); DM2, MEMS DM (Boston Micromachines) are optically conjugated [by sets of the spherical-mirror—(Mn)-based telescopes] with the subject's eye pupil, X–Y scanners and the H-S wavefront sensor. The reference arm of the AO-OCT system is designed to match the path length of the sample arm. A fixation point is used to set the retinal location of the imaged structure.

morph (AOptix Technologies, Campbell, California) and $\sim$3.12 mm diameter pupil image for the MEMS] and an imaging pupil diameter for the eye of $\sim$6.67 mm. In the diffraction-limited case, this imaging diameter would result in a lateral resolution of less than 4 μm at the retina. The detection channel of the OCT system consists of a custom design spectrometer, allowing 2 mm axial depth in the eye. The system was constructed on a $1.5\,\text{m} \times 1.8\,\text{m}$ laboratory optical table.

As pointed out in a previous report,[19] our AO-OCT system uses the OCT imaging beam to record and correct wavefront aberrations (8% of the light backreflected from the eye is redirected by a pellicle beam splitter toward the H-S wavefront sensor), allowing truly real-time operation of AO correction and eliminating the need for additional light sources. An additional pellicle beam splitter is placed in front of the subject's eye (it reflects 8% of the transmitted light), allowing presentation of a freely positioned fixation point during AO-OCT imaging. Another feature of our system is the implementation of a bimorph DM to correct large amounts of defocus and astigmatism, eliminating the need for trial lenses to correct an individual subject's refractive errors up to ±3 D defocus range and up to ±1 D cylinder. The same mirror can also be used to shift axially the focus of the AO-OCT beam to achieve optimal lateral resolution of retinal structures of interest. The AO-OCT control system operates with two personal computers (PCs). The OCT PC drives the X–Y galvo scanners and reads OCT spectral data from the frame grabber connected to an ATMEL camera link line CCD camera (ATMEL Corp., San Jose, California, USA). The maximum scanning range of our scanners at the retinal plane is about ±0.75 mm ($\pm 2.25^\circ$). The OCT acquisition software allows real-time display of B scans and saves the last acquired volume. An AO PC reads lenslet-spot data from the H-S wavefront sensor CCD and drives an AO closed loop with two deformable mirrors working in a cascaded mode (one mirror at a time); simultaneous operation of both mirrors is not supported by our current AO software. Both mirrors are driven by the same AO software, at the same closed-loop frequency (16 Hz), but using a different system matrix based on separate calibrations for each DM. The AO-OCT system operator chooses which mirror is active and performs the AO correction. The larger-stroke bimorph DM from AOptix Technologies is used to correct for low-order aberrations and is always used as the first corrector, while the smaller-stroke MEMS DM from Boston Micromachines Corporation (Watertown, Massachusetts, USA) corrects residual aberrations that are still present after correction with the bimorph mirror.

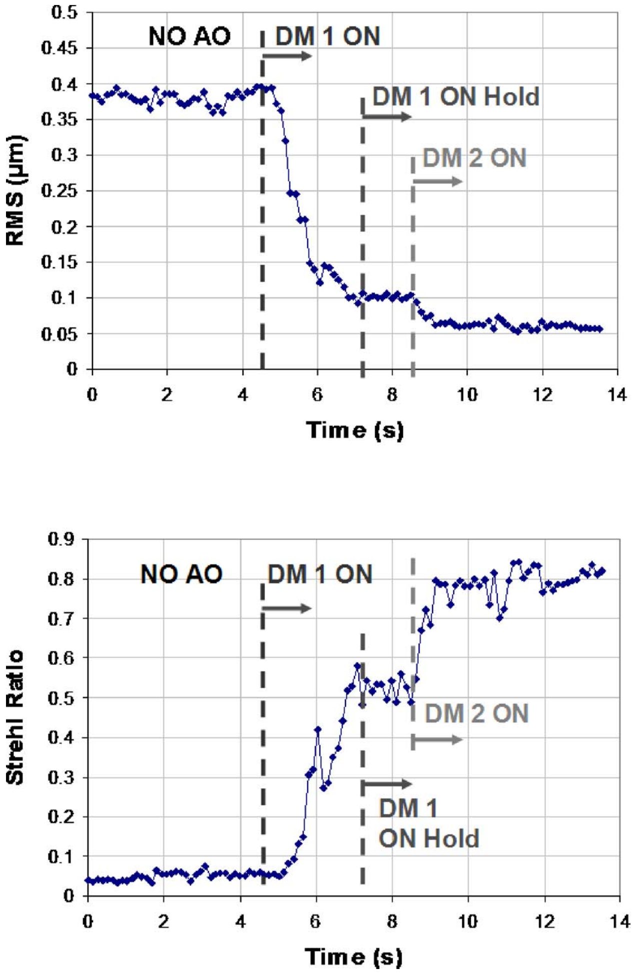

Fig. 2. (Color online) (Top) Example traces of the wavefront RMS in micrometers; (bottom) PSF Strehl ratio reconstructed from H-S centroid displacements (measured on a healthy volunteer's eye) plotted as a function of time for two-DM AO system operation.

B. Image Acquisition

A bite bar and forehead rest mounted on an X–Y–Z translation stage have been used for precise positioning of the eye and to minimize head movement. As already noted, a calibrated fixation point is used to position the eye for imaging at specified retinal locations as well as to reduce lateral eye motion. To ensure the maximum pupil size and minimize fluctuations in accommodation, the subject's eye was dilated and cyclopleged with 2.5% phenylephrine and 1% tropicamide. Before OCT data acquisition, the subject's eye aberrations were corrected with our two-DM AO system. As the first step, the MEMS DM was flattened and the bimorph DM was engaged to provide closed-loop correction for about 2–4 s. When the wavefront error was minimized, it was frozen and then AO correction was switched to the MEMS DM, which remained active during OCT acquisition. Root-mean-square (RMS) wavefront error was monitored during all these steps, and if an increase was observed we stopped OCT acquisition, flattened the MEMS DM, and started AO correction from the beginning. RMS of the wavefront error was used as a metric to evaluate AO subsystem performance. To evaluate statistically the performance of our two-DM AO system, a large number of subjects is required. This study is currently being performed and will be reported in a future publication.

Figure 2 shows an example of one subject's RMS wavefront error as seen in real time by the AO-OCT operator. It is clear in this example that the second DM improved the AO correction, although the RMS error does not reveal that this improvement was primarily in the higher-order aberration modes, which contribute relatively less than the lower-order modes to the overall RMS error. The improvement in correction is more evident from the Strehl ratio, plotted in the lower panel of Fig. 2.

To illustrate the effect of improved wavefront correction on OCT images, Fig. 3 shows three representative B scans acquired during AO acquisition using a protocol similar to the one presented in Fig. 2. From top to bottom, B-scans are shown without AO correction, with bimorph deformable mirror correction only, and with two-DM correction.

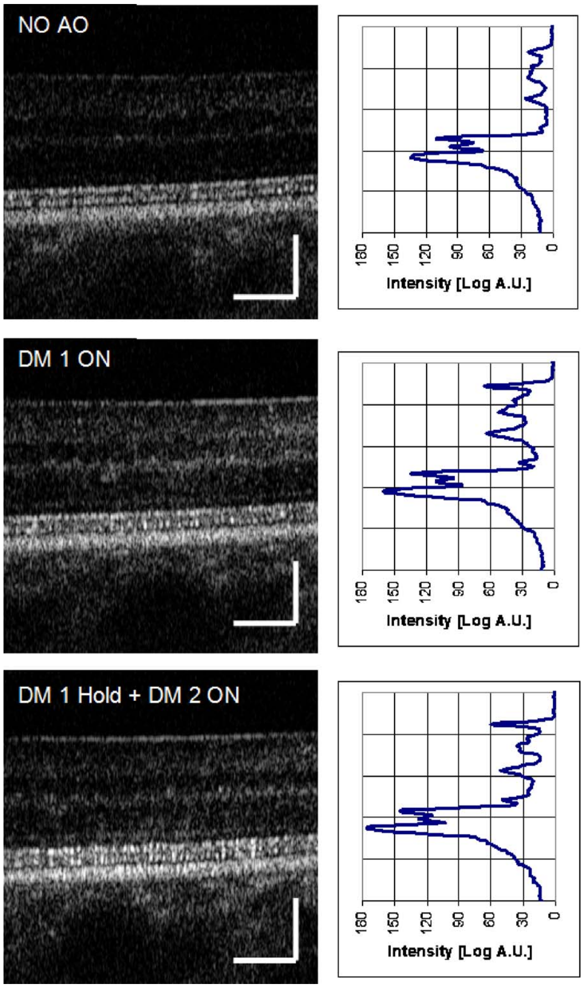

Fig. 3. (Color online) AO-OCT B-scans and corresponding averaged frame intensity profiles of the healthy retina acquired at 5° temporal retina. These frames have been picked arbitrarily from a movie acquired during the starting sequence of our AO system (an example is presented in Fig. 2). (Top) B-scan before correction, (middle) B-scan with DM1 correction only, (bottom) B-scan with DM1 on hold and DM2 active. Note increased intensity of photoreceptor layers and decrease in the depth of focus for improved wavefront error correction. Scale bar on the B-scans is 100 μm.

A 50 μs line exposure time was used to acquire all the AO-OCT data presented in this paper. Figure 3 illustrates improvement in visualization of the photoreceptors due to the improved Strehl ratio. The quality and details seen on B-scans with no AO correction of course varies between subjects, depending on their eye's aberration. The subject in Fig. 3 had minimal defocus and cylinder errors. In many cases where residual defocus and cylinder are present, the intensity of B-scans without AO correction is much lower.

The images presented here are based on two 3D AO-OCT acquisition modes: 1×1 mm ($3°\times 3°$) using 100 B-scans, or 250×400 μm ($0.75°\times 1.2°$) based on 400 B-scans with volume acquisition times of 5.6 s for both scanning modes. The corresponding frame rate of the large scanning mode was 18 frames/s (1000 lines/frame) and for the small scanning mode it was 72 frames/s (250 lines/frame). We used a triangular scanning pattern[20] for small volume acquisition only, which helps to reduce jittering effects observed on the fast-axis galvo scanner due to rapid change in the motion direction. We found our large scanning pattern to be useful in visualization of extended retinal structures (capillaries) and in creating an overview of an imaged area. It should be noted that the large AO-OCT volume covers less than 3% of the lateral area imaged with standard 3D FD-OCT systems[6–8] ($6\text{ mm}\times 6\text{ mm}$) but nevertheless allows registration with the fundus image or clinical 3D FD-OCT data. This implies that 36 AO-OCT locations should be imaged to reconstruct the area seen on clinical 3D FD-OCT. On the other hand, small scanning patterns proved to be essential for imaging cellular structures where subresolution sampling in both lateral dimensions is needed to see detailed structure. Because this scan pattern covers only 10% of the large AO-OCT scanning area and less than 0.3% of 3D FD-OCT, it is used mainly to provide a zoomed-in view of retinal structures of interest. Thus, 10 small AO-OCT volumes are needed to cover the large AO-OCT scanning area and 360 to cover the standard 3D FD-OCT scanning area. Table 1 summarizes parameters of 3D AO-OCT acquisition modes used in our experiments together with the standard volume acquisition mode used in clinical 3D FD-OCT systems.

The AO-OCT data presented in this paper have been acquired with FD-OCT software developed by Bioptigen, Inc. (Durham, North Carolina, USA). It displays acquired data in real time and allows storage of the "raw" data for-

Table 1. Volume Acquisition Modes of AO-OCT System versus Those of Current Clinical FD-OCT Systems

Scanning Mode	Scanned Area	Line/ B-Scan (Fast Axis)	B-Scans/ Volume (Slow Axis)	Line Exposure Time (μ_s)	Frame Rate (Frames/s)	Volume Acquisition Time (s)	Sampling Density (μm) Fast Lateral Axis	Sampling Density (μm) Slow Lateral Axis
3D FD-OCT	$6\text{ mm}\times 6\text{ mm}$	500–1000	100–200	~30–100	~9–54	~3–11	~6–12	~30–60
Large 3D AO-OCT	$1\text{ mm}\times 1\text{ mm}$	1000	100	50	~18	~5.6	~1	~10
Small 3D AO-OCT	$0.25\text{ mm}\times 0.4\text{ mm}$	250	400	50	~72	~5.6	~1	~1

mat (spectrum detected by CCD) and "processed" data. The images presented in this paper have been obtained from the raw data format saved by this software.

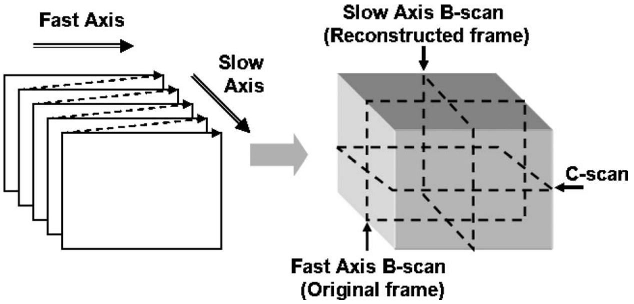
Fast Axis
Slow Axis
Slow Axis B-scan (Reconstructed frame)
C-scan
Fast Axis B-scan (Original frame)

Fig. 4. Orientation of fast- and slow-axis scans used for AO-OCT volume acquisition, and location of the cutting planes used in presentation of the volumetric data.

C. OCT Image Processing and Registration

For the best-quality OCT images, a series of signal processing steps must be performed.[12–14] This processing is carried out after the imaging session on the raw AO-OCT data using LABVIEW-based software developed in our laboratory. Postprocessing steps include subtraction of the spectrometer dc spectrum (to remove coherent noise), resampling of acquired spectra from wavelength to wavenumber space (including dispersion compensation), spectral shaping of the reconstructed spectrum (to create Gaussian-shaped spectrum), zero padding (to increase axial sampling after Fourier transformation), and inverse Fourier transformation. The resultant OCT images are then represented with a log intensity scale. To enhance the contrast of the final images, we set up 8-bit gray-scale .tif images so that 0.5% of the pixels are saturated. After

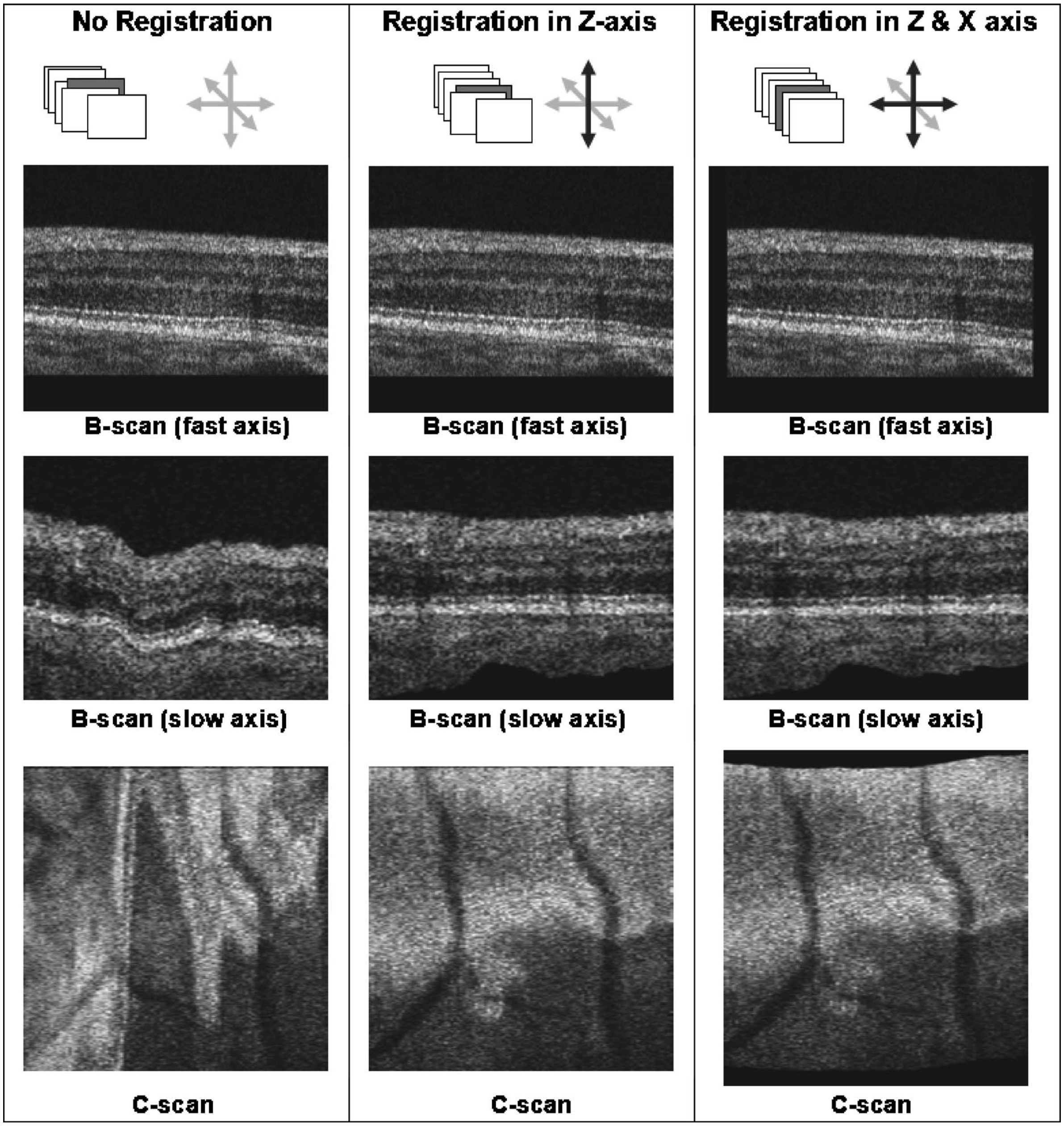
No Registration
Registration in Z-axis
Registration in Z & X axis
B-scan (fast axis)
B-scan (fast axis)
B-scan (fast axis)
B-scan (slow axis)
B-scan (slow axis)
B-scan (slow axis)
C-scan
C-scan
C-scan

Fig. 5. Examples of the B-scan self-registration algorithm performance presented on original B-scans (top), on reconstructed slow-axis B-scans (middle), and C-scans (bottom). Registered and unregistered axes are denoted by black and gray arrows, respectively.

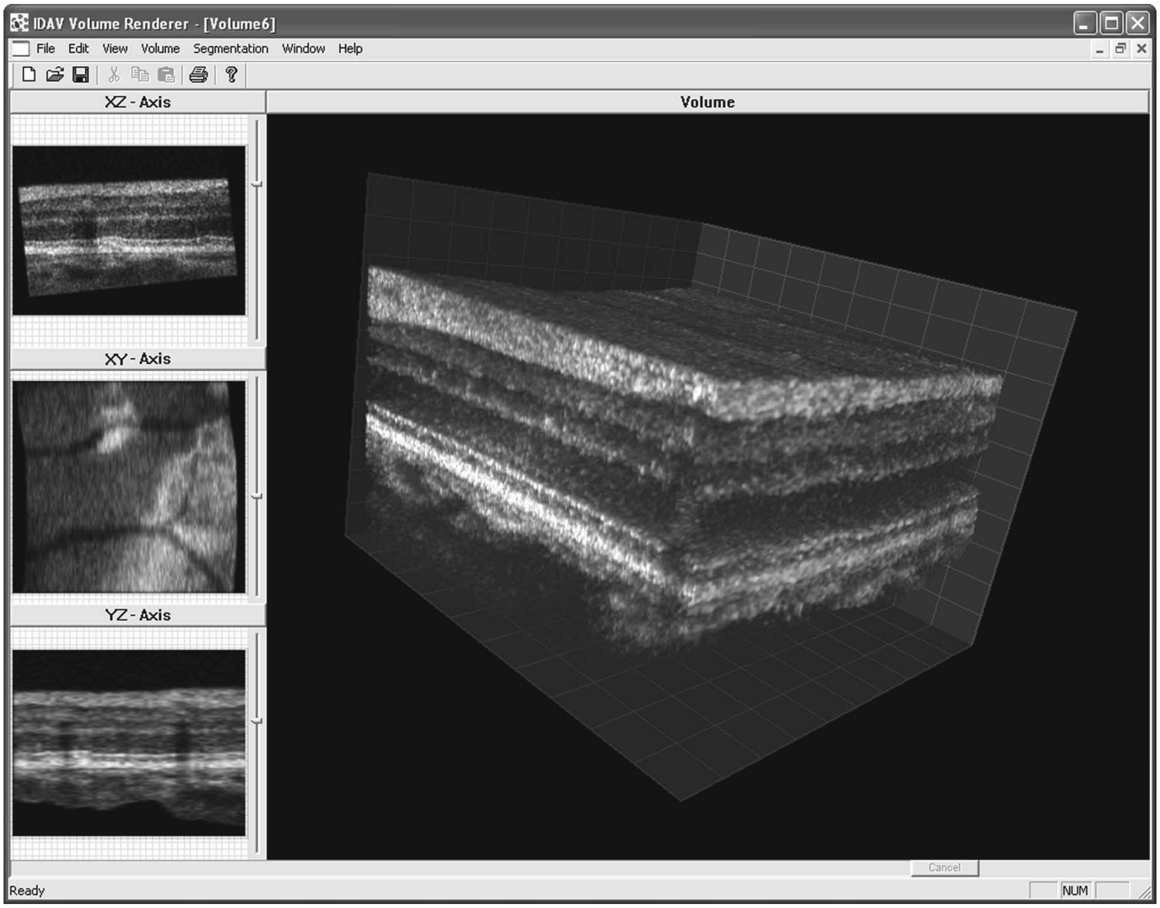
IDAV Volume Renderer - [Volume6]
File Edit View Volume Segmentation Window Help
XZ - Axis
XY - Axis
YZ - Axis
Volume
Cancel
Ready
NUM

Fig. 6. Screen shot from IDAV volume renderer for visualizing retinal data. Small images on the left provide access to three independent planes that can be moved through the volume by a cursor; large image on the right shows the reconstructed volume.

all these steps, our volumetric data are stored as a set of high-resolution .tif frames that can be optionally rendered as a movie. Figure 4 shows a schematic volumetric image acquisition and orientations of reconstructed frames. Two scanning axis orientations are presented, slow and fast, as well as orientations of corresponding original acquired B-scans, the slow-axis B-scan (plane created from an axial line located on consecutive fast-axis B-scans) and C-scan (plane created from a lateral line located on consecutive fast-axis B-scans) with respect to the acquired volume.

It is clear that by arranging acquired B-scans in consecutive order, one can create a volumetric representation of the imaged structure. Unfortunately, the resulting volumetric structure is often disrupted by eye and head motion due to relatively long volume acquisition time. These artifacts can be visualized easily on reconstructed slow-axis B-scans and C-scans, as illustrated by Fig. 4 depicting axial and lateral motion artifacts. Note that axial motion artifacts are clearly seen in both reconstructed planes and in slow-axis B-scans and C-scans, while lateral motion artifacts can be visualized only on the C-scans. To reduce this effect, we used a correlation-based algorithm to find displacements and respectively shift consecutive B-scans. In our standard registration procedure we used public domain software, IMAGE J (National Institutes of Health, Bethesda, Maryland, USA) with a frame correlating plug-in.[25] We have tested corrections of single-axis distortions (axial distortions) and two-axis distortions (axial and lateral distortions) and found that clear improvement allowing artifact-free reconstruction of volumetric data has been possible. Figure 5 illustrates frames reconstructed from the AO-OCT volume in the case of no correction (left column), single-axis correction (middle column) and two-axis correction (right column).

It should be noted that even single-axis correction drastically reduces motion artifacts, as can be seen by comparing the B-scan (slow axis) and C-scan reconstructed between the left and the middle columns. Reduction of the lateral motion artifact, however, can be observed only on the reconstructed C-scans. In this example, only minimal lateral distortions were present, as can be deduced by comparing C-scans in the middle and left columns. Thus, in this case the two-axis registration could be omitted. The amount of two-axis correction depends strongly on the lateral distortions and scanning pattern used in imaging and becomes essential for small AO-OCT volumes. No correction has been performed in the slow scanning axis direction. The self-registration of volumetric AO-OCT data is also valuable for subsequent analysis and visualization. Most important, it permits the precise position of the structure to be located within the retinal volume, a feature that is not possible with any other AO imaging modality, including the latest time-domain AO-OCT systems.

D. Data Visualization

We have developed several methods for visualizing our registered AO-OCT volumetric data. This includes custom volume-rendering software developed in collaboration with the UC Davis Institute for Data Analysis and Visualization (IDAV) that supports active interaction with the data (rotation, zooming, cutting planes).[26] It allows 2D virtual cuts through the volume to be viewed in three main planes (fast-axis B-scans, slow-axis B-scans, and C-scans). Figure 6 shows the operator's view using the IDAV volume renderer.

Similar to other investigators, we find that reconstructed C-scans are easier to interpret if they are displayed together with reference B-scans (slow or fast axis) depicting the axial location of displayed C-scans. We also use axial averaging of consecutive C scans to reduce speckle contrast and improve visualization of the microscopic structures. In our C-scan axial averaging method, a Gaussian mask is used as a weighting function with the number of C scans within its FWHM used as a parameter. Owing to oversampling in the axial direction [spacing between axial points after fast Fourier transform (FFT) is

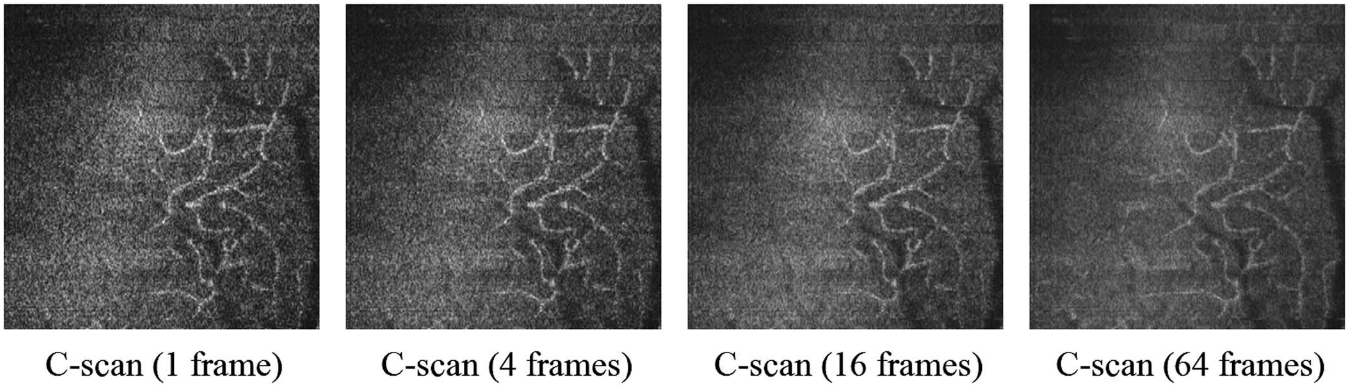

Fig. 7. C-scan of microvasculature reconstructed from retinal volume (1 m × 1 m) with intensity calculated by axial averaging. Each image illustrates averaging of different numbers of C-scans (0, 4, 16, or 64 frames). The foveolar center is located at the upper left corner.

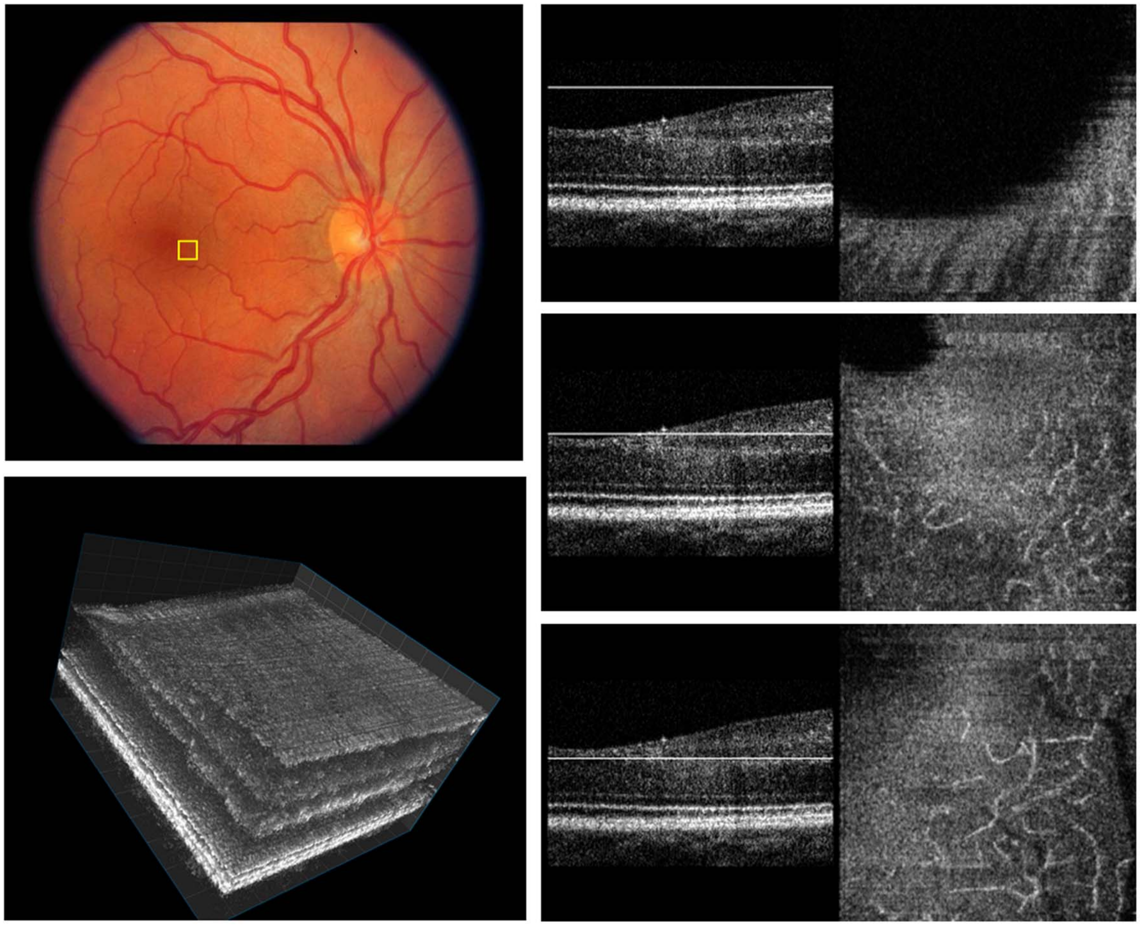

Fig. 8. (Color online) C-scan visualization of retinal capillaries and foveal avascular zone (1.5° nasal, 1.5° inferior retina). Square in fundus photo shows estimated location of the retinal volume in the panel below. The three figures on the right each show identical B-scans with a white line to illustrate the position of the corresponding C-scan.

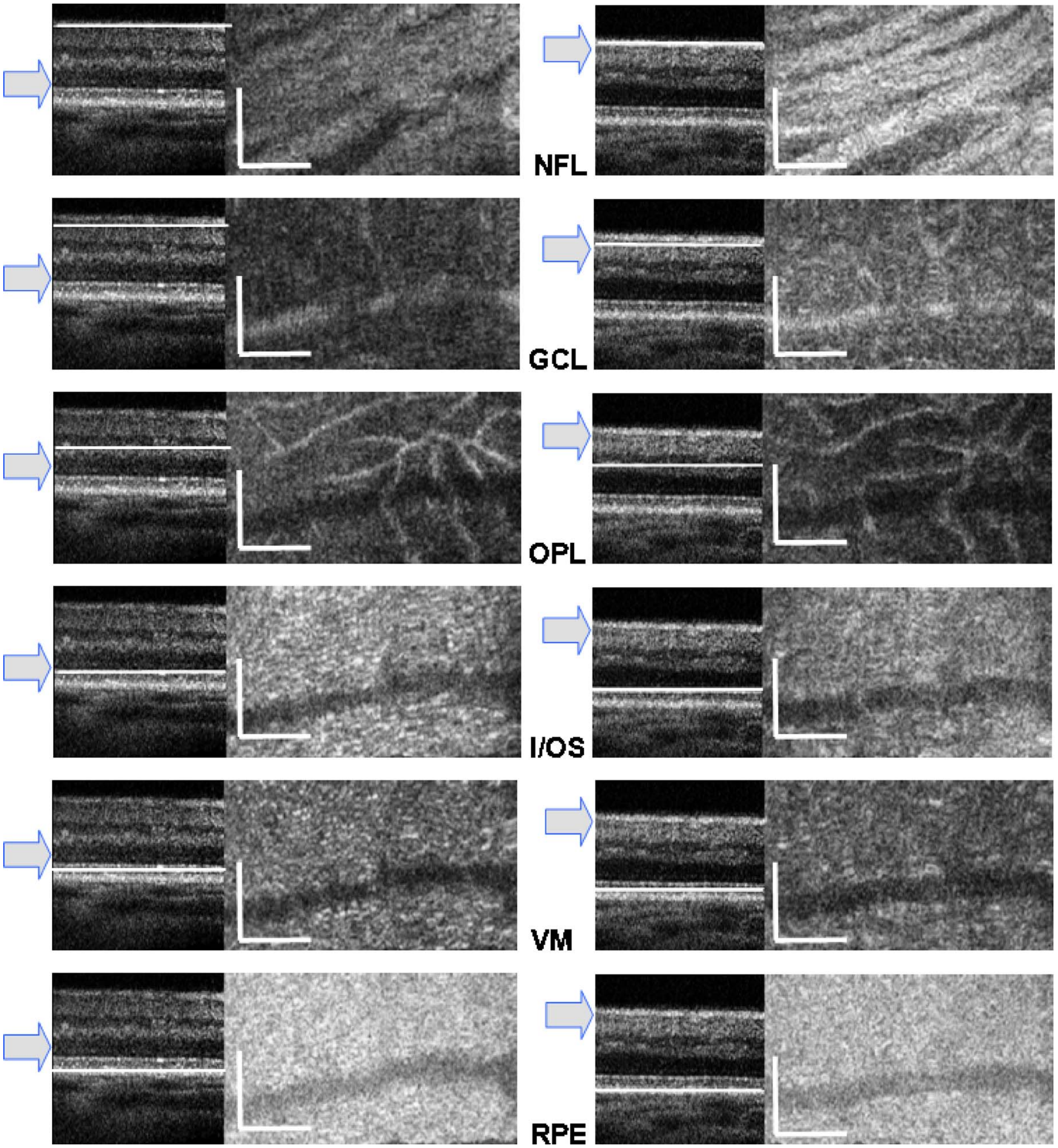

Fig. 9. (Color online) Reconstructed slow-axis B-scans and C-scans from two retinal volumes acquired with the focus set on photoreceptor layers (left column) and on upper retinal layers (right column). Arrow in each panel denotes estimated focus position. Rows show C-scan reconstruction of the same retinal layer (denoted by abbreviations) with the exact position indicated by a white line on the B-scan. Retinal layers in C-scans from top to bottom are nerve fiber layer (NFL), ganglion cell layer (GCL), outer plexiform layer (OPL), inner/outer segment junction (I/OS), Verhoeff's membrane (VM), and retinal pigmented epithelium (RPE). Scale bars = 100 μm (vertical and horizontal).

$\sim 1\ \mu$m], an average of four layers (within the mask FWHM) does not reduce axial resolution. Figure 7 shows C-scans with no averaging (C-scan thickness, $\sim 1\ \mu$m), 4-frame average (C-scan thickness, $\sim 4\ \mu$m), 16-frame average (C-scan thickness, $\sim 16\ \mu$m), and 64-frame average (C-scan thickness, $\sim 64\ \mu$m). This method could be used to reconstruct AO-SLO-like (SLO, scanning laser opthalmoscope) C-scans from AO-OCT volumetric data and may be useful in comparison of these two techniques. Figure 6 also illustrates the reduction in speckle contrast with increased numbers of averaged C scans. If too many frames are averaged, however, the contrast of observed structures is reduced.

3. RESULTS AND DISCUSSION

More than 25 volunteers have been tested with our AO-OCT instrument, including subjects with both healthy and diseased eyes. In this section we present examples of the retinal structures that can be imaged *in vivo* with our AO-OCT system. These images have been processed and registered as described in the previous sections to increase image contrast and reduce motion artifacts.

A. Capillaries and Foveal Avascular Zone Imaging

High volumetric resolution of AO-OCT and the ability to register B-scan images to minimize the axial distortion in

3D structures make our system an excellent tool to visualize microcapillaries and to precisely locate their axial and lateral positions within the retinal layers. This cannot be measured with any other retinal imaging modality. Figure 8 shows (1) a 3D volumetric AO-OCT image taken at the parafoveal area of a young healthy volunteer, and (2) the C-scan reconstruction from the 3D volumetric AO-OCT image at different depths. The AO-OCT images were acquired with the large scanning pattern.

To maximize the contrast of specific layers or structures of interest, the OCT beam needs to be focused at the plane where the structure is present, in this case at the capillaries in the upper retinal layers. As already mentioned, this is performed automatically with our AO control software by setting its reference at the proper defocus.

B. Cellular Structure Imaging

To test the ability of AO-OCT for imaging retinal cellular structures, we used the small scanning pattern and the C scans (averaged over four axial frames) were reconstructed from volumetric data. To visualize the effect of axial focus position on imaged structures, two volumes from the same retinal location of the same subject's eye have been acquired with two focus positions: first, on the photoreceptor layer and then on upper retinal layers. As seen in Fig. 9, reconstructed C- scans show bundles of axons in the NFL; microscopic structures in the ganglion cell layer (GCL); capillaries in the outer plexiform layer (OPL), which look rather large at this magnification; inner/outer segment junction (I/OS); Verhoeff's membrane (VM), where tips of cone photoreceptor outer segments are enveloped by microvilli; and the retinal pigment epithelium (RPE).

These results clearly demonstrate that for maximum contrast it is essential to set the axial focus of AO-OCT at the plane that contains the structure of interest. Owing to the short depth of focus of the imaging beam ($<100\ \mu$m), one cannot observe all retinal layers in a single volume. Thus, 2 to 3 volumes should be acquired at a single retinal location to maintain maximum lateral resolution for structures of all retinal layers.

C. Visualization of Retinal Disease

As an example of imaging diseased retinal structures with AO-OCT, a volume of a giant druse acquired with the large scanning pattern, $1\ \text{mm} \times 1\ \text{mm}$, is shown in Fig. 10.

Large soft drusen ($\geq 63\ \mu$m) are a major risk factor for developing exudative macular degeneration.[27] Figure 9 was obtained from the right eye of an 80-year-old male with mild age-related macular degeneration (AMD). Ophthalmic examination had revealed slight RPE changes and several hard exudates near the fovea in both eyes. Both eyes were normal with respect to visual acuity (20/20), color vision (pseudoisochromatic plates and panel D-15 test), and visual fields (Humphrey 24-2). A fundus photograph from several years earlier showed several drusen at the same location (1° temporal and 1° inferior retina) where the giant druse was imaged. This implies that several drusen must have convolved into one giant druse over time. The AO-OCT image clearly confirms earlier findings[28,29] on the typical location of drusen within the retina (i.e., between the basement membrane of the RPE and Bruch's membrane) and the structural impact they have on the inner and outer segments of photoreceptors. One may clearly see that the junction between the inner and the outer segments of the photoreceptor is

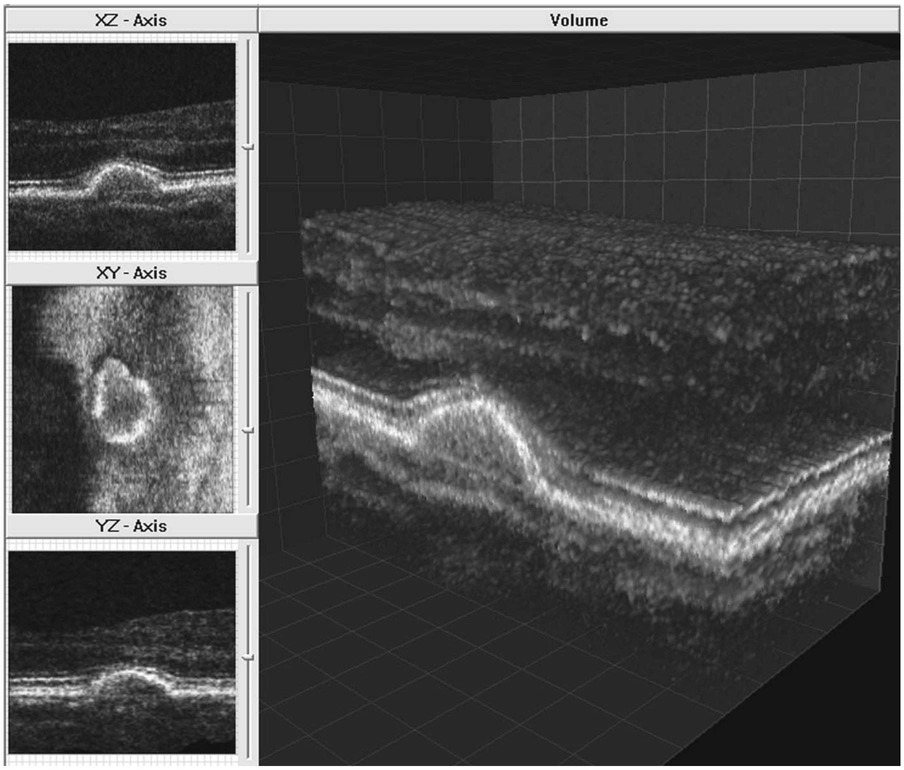

Fig. 10. Visualization of a microscopic druse in a patient with age-related macular degeneration. Details of the volume renderer as in Fig. 6.

blurred and mottled at the locations above the druse, whereas photoreceptors located farther away from the druse appear more defined and bright, indicating that there is some degree of disarray of photoreceptors caused by protrusion of the druse. Furthermore, the AO-OCT image reveals Bruch's membrane underneath the druse as well as the external limiting membrane (ELM), which appears as a dim line above the I/OS of the photoreceptor. Both the ELM and the I/OS of photoreceptors follow the contour of the druse, which may be a predictor of further disease progression.

4. CONCLUSIONS

We have shown that AO-OCT permits imaging of volumetric retinal structure with microscopic resolution. Several retinal structures previously imaged only by histology have been imaged with our AO-OCT instrument in living eyes. Owing to its higher axial and transverse resolution, AO-OCT is now able to reveal microscopic structures lying within any retinal layer. Registration of consecutive B-scans successfully reduces motion artifacts and allows volumetric reconstruction of C-scans from which one can obtain simultaneous presentation of corresponding B and C-scans at the same retinal depth. This is a significant step toward refining the way both clinicians and researchers analyze and study the retina and retinal changes. The ability to image cellular structures *in vivo* will facilitate structural correlations with retinal functions and diseases in real time.

We have successfully implemented the first two-DM AO system for retinal imaging with the capability of focusing at different retinal depths. This proved important for enhancing contrast of structures of interest, while also eliminating the complications of trial lenses for OCT. Both scanning patterns, $1\,\mathrm{mm}\times 1\,\mathrm{mm}$ and $0.25\,\mathrm{mm}\times 0.4\,\mathrm{mm}$, have proved to be useful in microstructure and cellular imaging, respectively.

One of the limitations of our current AO-OCT system is that we have so far not fully compensated for the chromatic aberrations of the eye.[22] As described in the introduction, one of the ways to overcome this limitation would be to use an achromatizing lens as proposed by Fernández *et al.*[23] These and other enhancements of AO-OCT will permit even more detailed *in vivo* visualization of cellular structures in the retina that have hitherto been seen only through histology.

ACKNOWLEDGMENTS

We gratefully acknowledge the contributions of Donald T. Miller, Barry Cense, Ravi Jonnal, Jungtea Rha, and Yan Zhang from the School of Optometry, Indiana University, Bloomington. Contributions of Joseph A. Izatt, Mingtao Zhao, Bradley A. Bower, and Marinko Sarunic from the Department of Biomedical Engineering, Duke University, Durham, North Carolina, are also gratefully acknowledged. The help of Alfred R. Fuller, David F. Wiley, and Bernd Hamann from the Institute for Data Analysis and Visualization (IDAV), UC Davis, for developing 3D visualization software; and Bioptigen Inc., Durham, North Carolina, for providing OCT data-acquisition software is appreciated. This research was supported by the National Eye Institute (EY 014743) and a Research to Prevent Blindness Jules and Doris Stein Professorship.

Corresponding author John S. Werner's e-mail address is jswerner@ucdavis.edu; phone, 916-734-6817; fax, 916-734-4543.

REFERENCES

1. A. F. Fercher, C. K. Hitzenberger, G. Kamp, and Y. Elzaiat, "Measurement of intraocular distances by backscattering spectral interferometry," Opt. Commun. **117**, 43–48 (1995).
2. G. Häusler and M. W. Lindner, "Coherence radar and spectral radar—new tools for dermatological diagnosis," J. Biomed. Opt. **7**, 21–31 (1998).
3. M. Wojtkowski, R. Leitgeb, A. Kowalczyk, T. Bajraszewski, and A. F. Fercher, "*In vivo* human retinal imaging by Fourier domain optical coherence tomography," J. Biomed. Opt. **7**, 457–463 (2002).
4. M. Wojtkowski, T. Bajraszewski, P. Targowski, and A. Kowalczyk, "Real time *in vivo* imaging by high-speed spectral optical coherence tomography," Opt. Lett. **28**, 1745–1747 (2003).
5. N. A. Nassif, B. Cense, B. H. Park, M. C. Pierce, S. H. Yun, B. E. Bouma, G. J. Tearney, T. C. Chen, and J. F. de Boer, "*In vivo* high-resolution video-rate spectral-domain optical coherence tomography of the human retina and optic nerve," Opt. Express **12**, 367–376 (2004).
6. M. Wojtkowski, V. Srinivasan, J. G. Fujimoto, T. Ko, J. S. Schuman, A. Kowalczyk, and J. S. Duker, "Three-dimensional retinal imaging with high-speed ultrahigh-resolution optical coherence tomography," Ophthalmology **112**, 1734–46 (2005).
7. U. Schmidt-Erfurth, R. A. Leitgeb, S. Michels, B. Považay, S. Sacu, B. Hermann, C. Ahlers, H. Sattmann, C. Scholda, A. F. Fercher, and W. Drexler, "Three-dimensional ultrahigh-resolution optical coherence tomography of macular diseases," Invest. Ophthalmol. Visual Sci. **46**, 3393–3402 (2005).
8. S. Alam, R. J. Zawadzki, S. Choi, C. Gerth, S. S. Park, L. Morse, and J. S. Werner, "Clinical application of rapid serial Fourier-domain optical coherence tomography for macular imaging," Ophthalmology **113**, 1425–31 (2006).
9. J. F. de Boer, B. Cense, B. H. Park, M. C. Pierce, G. J. Tearney, and B. E. Bouma, "Improved signal-to-noise ratio in spectral-domain compared with time-domain optical coherence tomography," Opt. Lett. **28**, 2067–2069 (2003).
10. R. Leitgeb, C. K. Hitzenberger, and A. F. Fercher, "Performance of Fourier domain vs. time domain optical coherence tomography," Opt. Express **11**, 889–894 (2003).
11. M. A. Choma, M. V. Sarunic, Ch. Yang, and J. A. Izatt, "Sensitivity advantage of swept source and Fourier domain optical coherence tomography," Opt. Express **11**, 2183–2189 (2003).
12. R. A. Leitgeb, W. Drexler, A. Unterhuber, B. Hermann, T. Bajraszewski, T. Le, A. Stingl, and A. F. Fercher, "Ultrahigh resolution Fourier domain optical coherence tomography," Opt. Express **12**, 2156–2165 (2004).
13. B. Cense, N. A. Nassif, T. C. Chen, M. C. Pierce, S.-H. Yun, B. H. Park, B. E. Bouma, G. J. Tearney, and J. F. de Boer, "Ultrahigh-resolution high-speed retinal imaging using spectral-domain optical coherence tomography," Opt. Express **12**, 2435–2447 (2004).
14. M. Wojtkowski, V. J. Srinivasan, T. H. Ko, J. G. Fujimoto, A. Kowalczyk, and J. S. Duker, "Ultrahigh-resolution, high-speed, Fourier domain optical coherence tomography and methods for dispersion compensation," Opt. Express **12**, 2404–2422 (2004).
15. D. T. Miller, J. Qu, R. S. Jonnal, and K. Thorn, "Coherence gating and adaptive optics in the eye," Proc. SPIE **4956**, 65–72 (2003).
16. B. Hermann, E. J. Fernandez, A. Unterhubner, H. Sattmann, A. F. Fercher, W. Drexler, P. M. Prieto, and P.

Altai, "Adaptive-optics ultrahigh-resolution optical coherence tomography," Opt. Lett. **29**, 2142–2144 (2004).

17. Y. Zhang, J. Rha, R. Jonnal, and D. Miller, "Adaptive optics parallel spectral domain optical coherence tomography for imaging the living retina," Opt. Express **13**, 4792–4811 (2005).
18. E. Fernández, B. Považay, B. Hermann, A. Unterhuber, H. Sattman, P. Prieto, R. Leitgeb, P. Anhelt, P. Artal, and W. Drexler, "Three-dimensional adaptive optics ultrahigh-resolution optical coherence tomography using liquid crystal spatial light modulator," Vision Res. **45**, 3432–3444 (2005).
19. R. J. Zawadzki, S. M. Jones, S. S. Olivier, M. Zhao, B. A. Bower, J. A. Izatt, S. Choi, S. Laut, and J. S. Werner, "Adaptive-optics optical coherence tomography for high-resolution and high-speed 3D retinal *in vivo* imaging," Opt. Express **13**, 8532–8546 (2005).
20. Y. Zhang, B. Cense, J. Rha, R. S. Jonnal, W. Gao, R. J. Zawadzki, J. S. Werner, S. Jones, S. Olivier, and D. T. Miller, "High-speed volumetric imaging of cone photoreceptors with adaptive optics spectral-domain optical coherence tomography," Opt. Express **14**, 4380–4394 (2006).
21. D. Merino, C. Dainty, A. Bradu, and A. G. Podoleanu, "Adaptive optics enhanced simultaneous *en-face* optical coherence tomography and scanning laser ophthalmoscopy," Opt. Express **14**, 3345–3353 (2006).
22. E. Fernández and W. Drexler, "Influence of ocular chromatic aberration and pupil size on transverse resolution in ophthalmic adaptive optics optical coherence tomography," Opt. Express **13**, 8184–8197 (2005).
23. E. J. Fernández, A. Unterhuber, B. Považay, B. Hermann, P. Artal, and W. Drexler, "Chromatic aberration correction of the human eye for retinal imaging in the near infrared," Opt. Express **14**, 6213–6225 (2006).
24. S. P. Laut, S. M. Jones, S. S. Olivier, and J. S. Werner, "Scanning laser ophthalmoscope design with adaptive optics," Proc. SPIE **6007**, 60070I (2005).
25. P. Thévenaz, U. E. Ruttimann, and M. Unser, "A pyramid approach to subpixel registration based on intensity," IEEE Trans. Image Process. **7**, 27–41 (1998).
26. R. J. Zawadzki, A. R. Fuller, M. Zhao, D. F. Wiley, S. S. Choi, B. A. Bower, B. Hamann, J. A. Izatt, and J. S. Werner, "3D OCT imaging in clinical settings: toward quantitative measurements of retinal structures," Proc. SPIE **6138**, 1–11 (2006).
27. R. Klein, B. E. Klein, S. C. Tomany, S. M. Meuer, and G. H. Huang, "Ten-year incidence and progression of age-related maculopathy: the Beaver Dam eye study," Ophthalmology **109**, 1767–79 (2002).
28. S. H. Sarks and J. P. Sarks, "Age-related maculopathy: nonneovascular age-related macular degeneration and the evolution of geographic atrophy," in *Retina*, A. P. Schachat, ed. (Mosby, 2001), Vol. 2, pp. 1064–1099.
29. P. T. Johnson, G. P. Lewis, K. C. Talaga, M. N. Brown, P. J. Kappel, S. K. Fisher, D. H. Anderson, and L. V. Johnson, "Drusen-associated degeneration in the retina," Invest. Ophthalmol. Visual Sci. **44**, 4481–4488 (2003).